Light-Based Printing of Leachable Salt Molds for Facile Shaping of Complex Structures

Kleger, Nicole; Fehlmann, Simona; Lee, Seunghun S.; Dénéréaz, Cyril; Cihova, Martina; Paunović, Nevena; Bao, Yinyin; Leroux, Jean Christophe; Masania, Kunal; More Authors

DOI
10.1002/adma.202203878

Publication date
2022

Document Version
Final published version

Published in
Advanced Materials

Citation (APA)
Kleger, N., Fehlmann, S., Lee, S. S., Dénéréaz, C., Cihova, M., Paunović, N., Bao, Y., Leroux, J. C., Masania, K., & More Authors (2022). Light-Based Printing of Leachable Salt Molds for Facile Shaping of Complex Structures. *Advanced Materials*, *34*(32), Article 2203878. https://doi.org/10.1002/adma.202203878

ADVANCED MATERIALS
www.advmat.de

Light-Based Printing of Leachable Salt Molds for Facile Shaping of Complex Structures

Nicole Kleger, Simona Fehlmann, Seunghun S. Lee, Cyril Dénéréaz, Martina Cihova, Nevena Paunović, Yinyin Bao, Jean-Christophe Leroux, Stephen J. Ferguson, Kunal Masania, and André R. Studart**

3D printing is a powerful manufacturing technology for shaping materials into complex structures. While the palette of printable materials continues to expand, the rheological and chemical requisites for printing are not always easy to fulfill. Here, a universal manufacturing platform is reported for shaping materials into intricate geometries without the need for their printability, but instead using light-based printed salt structures as leachable molds. The salt structures are printed using photocurable resins loaded with NaCl particles. The printing, debinding, and sintering steps involved in the process are systematically investigated to identify ink formulations enabling the preparation of crack-free salt templates. The experiments reveal that the formation of a load-bearing network of salt particles is essential to prevent cracking of the mold during the process. By infiltrating the sintered salt molds and leaching the template in water, complex-shaped architectures are created from diverse compositions such as biomedical silicone, chocolate, light metals, degradable elastomers, and fiber composites, thus demonstrating the universal, cost-effective, and sustainable nature of this new manufacturing platform.

1. Introduction

Shaping of matter into complex structures has been greatly advanced through the advent of additive manufacturing techniques. A crucial development in this field has been the design and formulation of resins or inks with a broad variety of material compositions.[1–4] This has turned 3D printing from a prototyping tool into a manufacturing platform for functional objects and devices in health,[5] energy,[6] architecture,[7] and robotic applications.[8] Using inks with self-assembling building blocks has expanded the capabilities of 3D printing techniques to the fabrication of structures with intricate hierarchical architectures and feature sizes below accessible printer resolution.[1,9–12] Despite these enticing achievements and promising prospects, many materials are still not directly 3D printable due to challenges in fulfilling the rheological, physical, and chemical requirements of extrusion- and light-based printing techniques.[13] In addition, the relative lack of reproducibility and reliability of additive processing has made it difficult to produce parts for critical applications such as aerospace and medical, where certification of microstructure and part integrity is paramount.

3D printed sacrificial molds and templates offer a universal approach to shape matter into complex architectures without rheological or chemical modification of the material of interest. The idea of such indirect additive manufacturing is to first print the sacrificial template into the desired negative geometry and then cast or deposit the material of interest before final removal of the template.[14–24] This manufacturing

N. Kleger, S. Fehlmann, K. Masania,[+] A. R. Studart
Complex Materials
Department of Materials
ETH Zürich
Zürich 8093, Switzerland
E-mail: k.masania@tudelft.nl; andre.studart@mat.ethz.ch

The ORCID identification number(s) for the author(s) of this article can be found under https://doi.org/10.1002/adma.202203878.

[+]Present address: Faculty of Aerospace Engineering, Delft University of Technology, Kluyverweg 1, Delft 2629 HS, Netherlands

DOI: 10.1002/adma.202203878

S. S. Lee, S. J. Ferguson
Institute for Biomechanics
Department of Health Science and Technology
ETH Zürich
Zürich 8093, Switzerland

C. Dénéréaz
Laboratory of Mechanical Metallurgy
Institute of Materials
EPFL Lausanne
Lausanne 1015, Switzerland

M. Cihova
SNSF Postdoctoral Fellow
London SW7 2AZ, UK

N. Paunović, Y. Bao, J.-C. Leroux
Institute of Pharmaceutical Sciences
Department of Chemistry and Applied Biosciences
ETH Zürich
Zürich 8093, Switzerland

strategy has enabled the fabrication of intricate structures from a wide range of materials at very different length scales. At the centimeter scale, binder-jetting printed sand or stereographically printed polymer molds have been utilized to fabricate complex metal parts by investment casting[17,21] and elastomer parts by casting silicone resins, respectively.[16,19] At the millimeter scale and below, two-photon polymerization has been exploited to print 3D polymer templates for the creation of metal and ceramic microlattices with exquisite architectures and mechanical properties.[25,26] In many of these processes, the template material needs to be dissolved with chemicals or thermally degraded at temperatures above 400 °C.[27,28] This often makes the process energy demanding and/or increases the probability of cracking or deformation of the templated material.

A cost-effective and sustainable strategy to circumvent the above-mentioned processing issues is to use conventional table salt, that is, sodium chloride (NaCl), as molds or templates. Because NaCl is non-toxic and readily dissolvable in water at ambient temperature, salt templates do not require excessive heating or toxic solvents to be removed and are broadly studied for biomedical applications.[29–33] These features also make them suitable templates for shaping temperature-sensitive materials, such as living materials, hydrogels, and polymers. Alternatively, the physical and mechanical stability of NaCl up to its melting temperature of 801 °C enables infiltration of materials at elevated temperature in the molten state.[34] Such versatility has allowed for the use of salt particles as pore-forming templates for the fabrication of a broad range of materials, from aluminum foams for structural applications[35] to porous hydrogels for tissue engineering.[29,30] Beyond templating particles, salt has also been deposited around 3D printed polymeric templates to create castable molds upon polymer removal.[17,21] Only recently, we have enabled the direct printing of NaCl into 3D grid-like structures for the fabrication of magnesium with unique porous architectures.[36] Through rheological engineering, we unlocked 3D printing of NaCl for extrusion-based direct ink writing, which is however limited in both, the attainable resolution and freedom of architectural design. Novel approaches to manufacture complex-shaped salt templates are highly demanded.

Here, we report a versatile manufacturing platform for the light-based 3D printing of salt objects and their use as templates for the creation of complex-shaped structures of a wide range of materials. Salt-based objects with intricate geometry are printed from photocurable resins loaded with a high concentration of salt particles. Upon heat treatment, the object is converted into salt templates that can be infiltrated with the material of interest. To develop this platform, we have first studied ink formulations that satisfy the rheological requirements for 3D printing by stereolithography (SLA). Next, the effects of resin formulation on the printing parameters and printed feature sizes were systematically evaluated. This was followed by single-layer model experiments designed to investigate the mechanisms underlying the fabrication of crack-free salt templates. Finally, salt templates with 3D complex geometries were infiltrated with distinct materials across a broad range of material classes to demonstrate the potential and universal nature of this new additive manufacturing platform.

2. Results and Discussion

The additive manufacturing of complex-shaped objects using salt templates involves a series of processing steps that include light-based printing (i.e., vat photopolymerization), debinding, sintering, infiltration, and leaching processes (**Figure 1**a and Video S1, Supporting Information). The process is designed to generate a negative mold of dense salt that can be infiltrated with the material of interest and afterwards leached in water to create the desired complex-shaped object. Stereolithographic printing of the salt mold is achieved by suspending salt particles in a photo-curable resin. After fulfilling its shaping function during printing, the cured resin is thermally removed to provide a salt green body that is sintered into a dense negative mold at 690 °C. To facilitate the removal of the polymerized binder, a diluent phase is often incorporated in the resin formulation. Diluents are removed at an earlier stage of the debinding process and hence decrease the risk of cracking during removal of the polymerized phase. Due to the thermal stability of the salt, the negative mold can be infiltrated by liquified or molten materials at temperatures up to ≈720 °C, at which the material starts to soften. The final positive object is obtained upon cooling of the infiltrated template followed by simple dissolution of the salt phase in water at room temperature.

To illustrate the manufacturing process, we developed a photocurable ink comprising NaCl particles as salt, a mixture of monomer and crosslinker as reactive phase, camphor as non-reactive diluent, a commercially available photoinitiator (Omnirad 819), a photo-absorber (Sudan I) and the surfactant bis(2-ethylhexyl) sulfosuccinate sodium salt (AOT). Isobornyl acrylate (IBOA) is used as the main, monofunctional monomer, whereas the trifunctional monomer trimethylolpropane triacrylate (TMPTA) is employed as a crosslinker (Figure S1, Supporting Information). The mixture of monofunctional monomer, crosslinker, and photoinitiator enables light-induced polymerization of the illuminated areas during stereolithographic printing. The photo-absorber controls the light penetration into the ink and thereby impacts the resolution and speed of the printing process. The surfactant is used to disperse the hydrophilic salt particles in the hydrophobic liquid medium and later serves as a sintering aid for the densification of the printed objects (Figure S2, Supporting Information).

A key requirement of the process is to produce a dense, crack-free salt template at the end of the sintering step. Cracking is a common challenge in ceramic printing, and may result from internal mechanical stresses developed during shrinkage of the printed object upon calcination and sintering. To reduce shrinkage and minimize cracking, the concentration of salt particles in the initial resin should be maximized without impairing the rheological properties needed for the stereolithographic printing process. More specifically, in terms of rheological behavior, the ink must be sufficiently fluid to replenish the print stage under the action of gravity. Previous studies have shown that this flowability is achieved if at a shear rate of 30 s^{-1} the yield stress and apparent viscosity of the ink are kept below 10 Pa and 60 Pa s, respectively.[37,38]

In order to establish a formulation that satisfies the above criteria, we evaluated the effect of the concentration of salt particles, surfactant, and diluent on the rheological properties of the

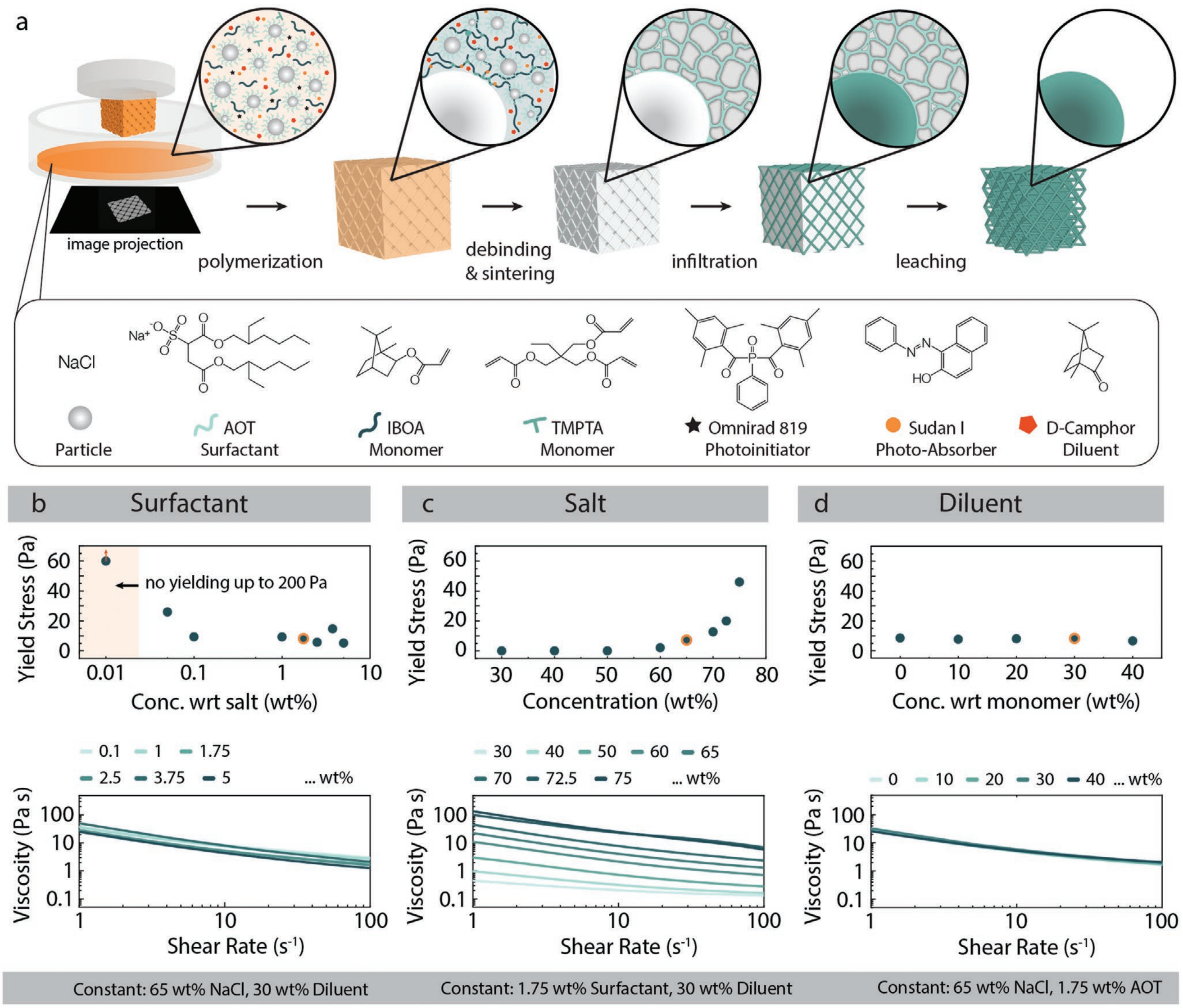

Figure 1. Overview of the manufacturing workflow and rheological characterization of salt-containing inks. a) Schematics depicting the layer-by-layer stereolithographic printing of a resin containing NaCl particles, surfactant, photocurable monomers, photo-absorber, photoinitiator, and a non-reactive diluent. The printed body is calcined to remove the organics and further sintered to obtain a dense, binderless NaCl body. This mold is infiltrated by a desired material and finally leached to obtain the positive complex-shaped body. b–d) The influence of the b) surfactant, c) salt, and d) diluent concentrations on the yield stress and apparent viscosity of the inks. No yielding is observed for inks with surfactant concentrations below 0.1 wt% (with respect to NaCl), which makes them unsuitable for the printing process. Orange encircled data indicates the optimal composition that was identified.

photocurable ink. The rheological measurements revealed that the yield stress and the apparent viscosity, defined as the ratio between shear stress and shear rate, of the ink strongly depend on the surfactant (AOT) and salt concentration (Figure 1b,c). A minimum surfactant content of 0.1 wt% is needed to lower the attractive van der Waals forces between the salt particles and thus reduce the yield stress and the viscosity of the ink below the rheological limits set by the printing process. For inks containing 1.75 wt% AOT, a percolating particle network with well-defined yield stress and high apparent viscosity is starting to form for salt concentrations above 60 wt%. This imposes an upper limit of 65 wt% for the maximum salt content that can be incorporated in the resin. The partial replacement of the monomer mixture by a diluent at up to 40 wt% does not affect the apparent viscosity and yield stress, suggesting that the rheological properties of the investigated ink are dominated by the interactions between the salt particles (Figure 1d). On the basis of this rheological analysis, a formulation with 65 wt% salt, 1.75 wt% surfactant with respect to NaCl, and 30 wt% of diluent with respect to monomer was chosen as a standard ink for the stereolithographic printing process as identified by the orange encircled data in Figure 1b–d.

After selecting the salt, diluent, and surfactant concentrations leading to rheological properties suitable for stereolithographic printing, we turned our attention to the optimization of the monomer mixture of the resin to enable controlled curing under the illumination conditions imposed by the printer. The composition of the monomer mixture, particularly the

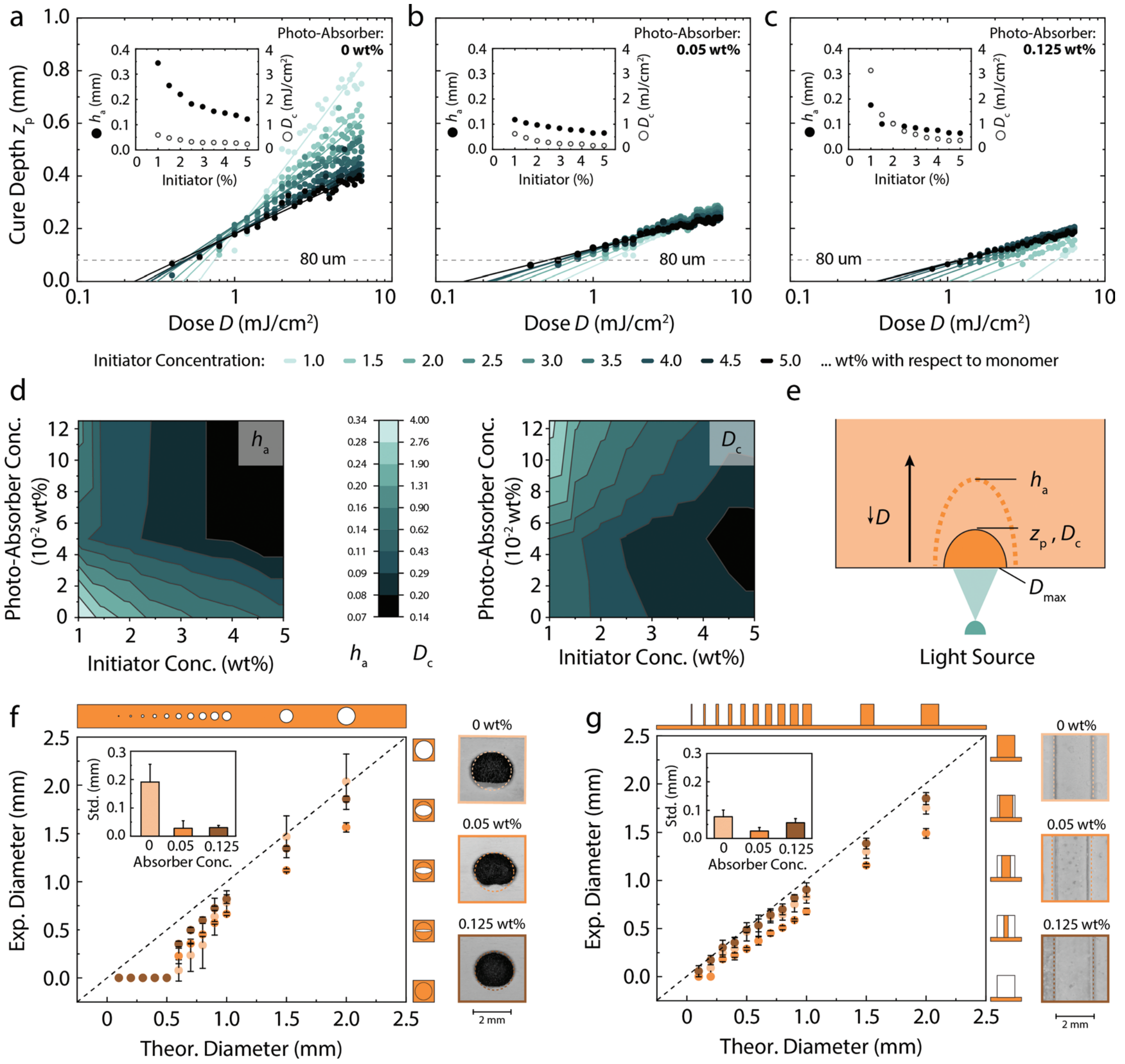

Figure 2. Photo-polymerization behavior and printing fidelity of salt-containing resins. a–c) The influence of the applied light dose (D_{max}) on the cure depth (z_p) of inks containing initiator concentrations in the range 1–5 wt% with respect to monomer. Fixed photo-absorber contents of a) 0 wt%, b) 0.05 wt%, and c) 0.125 wt% are used in these experiments. The corresponding light penetration depth (h_a) and critical dose (D_c) obtained by fitting the modified Beer-Lambert law to the experimental data are indicated in the insets. The results are summarized in d) to highlight the effect of the photo-absorber and photo-initiator concentrations on h_a and D_c. e) 2D sketch defining the parameters analyzed and illustrating the region of the ink that is illuminated with a dose equal or higher than D_c (dark orange). f,g) Printing fidelity of inks with 0, 0.05, and 0.125 wt% photo-absorber for f) negative and g) positive features printed at a cure depth (h_a) of 80 µm. The insets depict the average standard deviation of all size measurements (0–2 mm) for different photo-absorber concentrations. Optical microscopy images show representative examples of the 2 mm designed features, whereas the dashed lines indicate the theoretical size thereof.

concentration of the photo-absorber and photoinitiator, affects the polymerization process by determining the penetration of light into the ink and the concentration of reactive species created upon illumination.

To quantify these correlations, we studied the effect of the ink composition on the polymerization process by measuring the resulting thickness of cured ink as a function of the light dose for formulations with varying concentrations of photoinitiator and photo-absorber (**Figure 2**). In these single-layer experiments, the photoinitiator content was changed between 1 and 5 wt% (with respect to monomer), whereas the concentration of photo-absorber was varied in the range 0–0.125 wt% (with respect to monomer). Both weight percentage ranges are defined as a weight fraction with respect to the combined mass of both monomers, IBOA and TMPTA. The experimental data obtained reveal that the thickness of the polymerized layer (z_p), also referred to as cure depth, changes with the applied light dose (D_{max}) in a logarithmic fashion, as expected from the modified Beer–Lambert law: $z_p = h_a \ln(D_{max}/D_c)$, where h_a is the light penetration depth and D_c is the critical light dose to initiate polymerization.[39] The fact that the experimental data follow this theoretical scaling indicates that the assumption of an optically homogenous medium underlying this simple model is fulfilled in this case despite the heterogeneous nature of the particle-filled resin. By fitting the Beer–Lambert equation to the experimental data, we use this simple model for different resin formulations to quantify the light penetration depth (h_a) and the critical dose (D_c) from the slope and x-axis intercept in a semi-$\log_e$ plot, respectively (Figure 2a–c).[39]

The effect of the initiator and photo-absorber on h_a and D_c are directly influenced by the concentrations of photon-absorbing and reactive species present in the ink. Taking the formulation without photo-absorber (0 wt% Sudan I) as an example, we find that an increase in initiator concentration reduces h_a substantially while keeping the D_c value nearly constant (inset to Figure 2a). The drop in light penetration results from the fact that the initiator molecules are photon-absorbing species. The nearly constant D_c value suggests that the initiator concentration of 1 wt% is already sufficient to generate a high density of reactive monomer species for the polymerization process. Altered trends are observed when 0.125 wt% photo-absorber is added to the resin (Figure 2c). In this case, the photo-absorbing molecules dominate the light penetration depth, keeping the h_a values low for most of the initiator concentrations tested. The presence of a high photo-absorber concentration in this resin decreases the relative fraction of activated photo-initiators in the mixture, which is translated into a much stronger effect of the initiator concentration on the critical dose.

By collecting the data from such photo-polymerization analysis in iso-line plots, we obtained an experimental map that provides useful guidance for the formulation of inks with well-defined light penetration depth and critical dose (Figure 2d). In terms of critical dose, inks with low D_c are often desired to reduce the printing time. Since the printer operates at a fixed illumination intensity, a lower critical dose reduces the time the ink needs to be illuminated to generate the concentration of reactive species required for polymerization. With regards to the light penetration depth, formulations with low h_a show a weaker dependence of the cure depth on the illumination dose. This makes the inks more stable against possible variations in the illumination dose resulting from manufacturing issues, potentially improving the reproducibility of the printing process.

To evaluate the effect of the resin formulation on the fidelity and reproducibility of the SLA printing process, we printed model parts with positive or negative features and compared the experimentally obtained sizes with their nominal theoretical values (Figure 2f,g). Experiments were performed with inks containing a fixed initiator concentration of 2 wt% and varying photo-absorber contents of 0, 0.05, and 0.125 wt%. This allowed us to evaluate inks with different sets of D_c and h_a values for their printing accuracy and reproducibility. By comparing experimental and nominal sizes, we find that the fidelity of negative features is high for dimensions greater than 1 mm (Figure 2f). The opposite is true for positive features, which show sizes closer to their nominal values when smaller than 1 mm (Figure 2g). While the size accuracy was shown to depend on the exact composition of the ink, most formulations lead to very reproducible feature dimensions, as reflected in the low standard deviation values obtained. The exception to this trend is the ink prepared without light-absorber when used to print negative features. In this case, the strong dependence of the polymerization depth (z_p) on the applied light dose (D_{max}) leads to poorly reproducible negative features across a broad size range (Figure 2f). To combine fast printing, high fidelity, and high reproducibility, an ink formulation with 0.05 wt% photo-absorber and 2 wt% photoinitiator that lead to low h_a and D_c values was selected for the stereolithographic printing of the salt-laden parts.

Salt-laden objects with complex geometries were successfully printed using the optimized ink formulation (**Figure 3**a). To establish the calcination and sintering procedures required to convert the printed parts into dense salt templates, we conducted thermogravimetric analysis (TGA) of selected polymerized samples (Figure S3a, Supporting Information). The TGA data show that samples with diluent undergo a mild weight loss of 7.4% when heated up to about 230 °C, which is followed by a sequence of mass drops reaching in total of 32.3% at 430 °C. Combined with differential scanning calorimetry (DSC, Figure S3b, Supporting Information), these results suggest that small amounts of unreacted monomers and camphor are removed from the sample below 230 °C, followed by the evaporation of unreacted monomers up to 280 °C. Further heating above this temperature results in the thermal decomposition of the polymerized organic phase. Comparison between samples with and without 30 wt% camphor indicates that this compound sublimates from the polymerized resin at temperatures between 85 and 240 °C.

The fabrication of crack-free salt templates after calcination and sintering was experimentally found to require the presence of 30 wt% of camphor as a diluent in the ink (with respect to monomer). To better understand the role of camphor in preventing cracking of the printed object during calcination, we examined the microstructure of the polymerized ink after heat treatment at 200 and 690 °C. In these experiments, cracks were quantified by image analysis of cracked area in printed cubes of different sizes imaged under transmitted light (Figure 3b, top). In line with previous studies,[2,40] the addition of 30 wt% diluent was found to significantly reduce cracking of the sample upon heating, decreasing the imaged cracked area of sintered 1 cm cubes from approximately 2.9% to values below 0.6% (Figure 3b, bottom).

Surprisingly, we discovered that the beneficial effect of camphor does not arise predominantly from its expected role in generating open pores upon sublimation to facilitate the removal of thermally degraded polymer at higher temperatures. Instead, experiments with the camphor-free inks show that extensive cracking is already observed when the sample is heated up to 200 °C (Figure 3b), which is significantly lower than the thermal degradation temperature of the polymer (270–430 °C). By further increasing the temperature to 690 °C, we even detected a partial closure of cracks, which reduce in area from 6.4% to 2.9% for 1 cm cubes without camphor.

Controlled experiments in single printed layers provide insightful hints into the possible effect of camphor in preventing extensive cracking during calcination at relatively low temperatures. In these experiments, we freely illuminated resins and inks for 40 s without the constrain of the print head to obtain single-layer stripes of 5 mm × 20 mm. Finally, we qualitatively assessed the extent of warpage of these single printed layers after drying at either room temperature or 200 °C. We hypothesized that internal stresses manifested as warpage in these model experiments may cause cracking of the multi-layered printed object during thermal treatment.

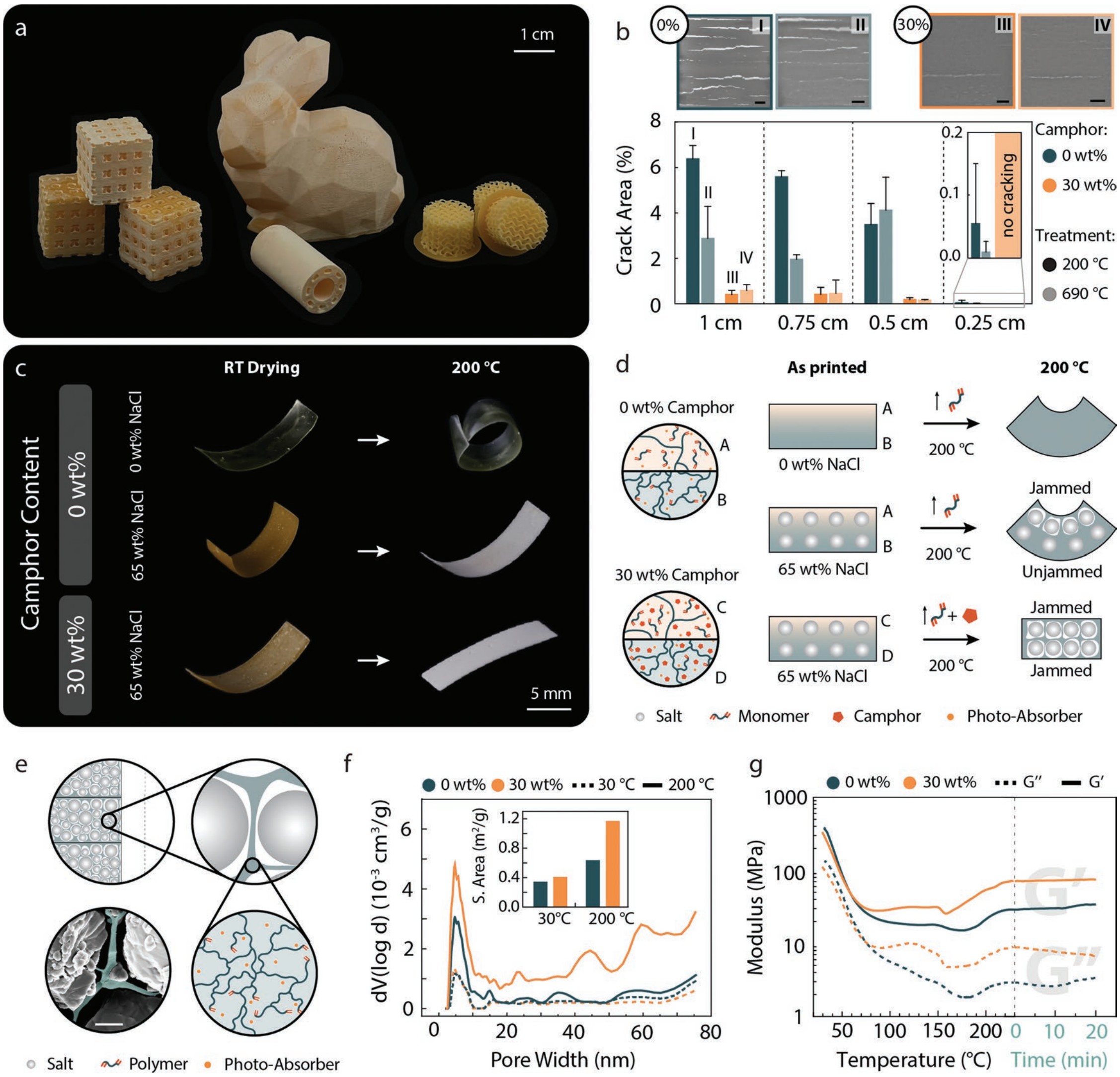

Figure 3. Shape complexity and cracking inhibition in salt-containing printed inks. a) Complex-shaped objects printed using optimized ink formulations. b) Measured cracked area in printed cubes of different side lengths after heat treatment at 200 °C (dark color) or 690 °C (bright color). Optical microscopy images in light transmission mode (top) illustrate the effect of 30 wt% camphor on the formation of cracks (bright areas). Scale bars: 1 mm. c) Shape changes upon drying of model layers printed using salt-containing resins with or without camphor. All model layers are illuminated on the bottom side, and a salt-free resin (top row) is used as control. d) Proposed mechanism for crack inhibition in inks containing camphor and salt particles. The drawings indicate the distinct crosslinking densities and amount of residual monomer expected at the bottom (B,D) and top (A,C) of a single printed layer. e) Schematics showing the presence of a percolating network of salt particles resulting from the shrinkage of the polymer continuous phase upon heating of the printed material to 200 °C. Shrinkage of the polymer phase (blue) beyond particle jamming results in detachment from the particles and the formation of interstitial pores, as indicated in the false-colored SEM image. Scale bar: 2 µm. f) Pore size distribution and total surface area (S. Area, BET Analysis, Inset) of printed inks without (blue) or with (orange) camphor after drying at 30 and 200 °C. g) Storage (*G*′) and loss (*G*″) moduli of printed bars subjected to DMA in torsion mode. Samples were heated to 230 °C, followed by an isothermal hold at 230 °C for 20 min.

Photographs of a polymerized sample without salt particles and camphor reveal strong warpage of the single-layer upon drying at ambient temperature, an effect that becomes even more pronounced at 200 °C (Figure 3c and Figure S4, Supporting Information). This suggests the presence of a gradient in monomer conversion and crosslinking density across the thickness of the layer (Figure 3d). Because of the lower illumination at the top of the layer (i.e., further away from the illumination source in the printing setup, see Figure 2e), this region likely contains a higher concentration of unreacted monomers compared to the directly exposed bottom side of the layer that is exposed to maximum dosage. Such a gradient in unreacted monomer concentration would translate into differential shrinkage of the layer during free monomer removal upon washing and drying, leading to the build-up of internal stresses and ultimately causes warpage.

The addition of salt particles to the camphor-free polymerized samples leads to even stronger warpage after room-temperature drying. Interestingly, the high initial warpage of such a layer reduces substantially when the sample is further heated to 200 °C. We interpret this effect as a result of jamming of the salt particles at the not directly illuminated top side of the layer, which restricts the shrinking during monomer evaporation due to the formation of a compressed load-bearing particle network. This leads to preferential shrinkage of the directly illuminated bottom side of the layer, partially compensating for the strong initial warpage. Importantly, our experiments show that the initial warpage of the layer can be fully reversed when camphor is added to the formulation. We assume that sublimation of camphor leads to sufficient shrinkage of the sample, such that particles at both sides of the layer become jammed. By providing a locking mechanism that is triggered via the sublimation of camphor, the salt particles prevent the build-up of differential stresses across the sample cross-section that causes cracking in the thermally treated printed objects.

Scanning electron microscopy (SEM) images from samples dried for 20 h at 200 °C confirm the strong shrinkage of the polymer phase and the formation of pores between the salt particles after the sublimation of the diluent (Figure 3e). With the help of nitrogen gas sorption analysis, we found that this porosity on the micrometer scale is complemented by presence of nanoscale pores in the range of 2–10 nm, as well as larger pores ranging from 20 to 75 nm in size (Figure 3f). Samples prepared with camphor show higher porosity and surface area compared to reference samples without camphor and those with removed camphor upon heat treatment at 200 °C (Figure 3f and Figure S5, Supporting Information). Because smaller nanopores are already present in camphor-free samples kept at 30 °C, the smaller nanopores are presumably part of the polymerized resin. Instead, the larger nanopores only appear upon drying at 200 °C and are therefore clearly associated with the removal of the diluent from the camphor-containing sample. Finally, the pores at the micrometer scale are generated due to the contraction of the polymer phase upon diluent sublimation. These pores are likely to facilitate the thermal decomposition of the polymer at higher temperatures.

The proposed microstructural locking effect induced by the removal of camphor is reflected in the evolution of the mechanical properties of the printed object upon heating (Figure 3g and Figure S6, Supporting Information). After an initial softening during heating to 100 °C, the storage modulus (G') of the camphor-containing composite was found to increase from 31 to 75 MPa when the temperature was raised from 150 to 230 °C. This 1.5-fold increase in modulus contrasts with the 0.9-fold enhancement observed for the camphor-free sample within the same temperature interval. The higher stiffness of the composite prepared with camphor probably results from the formation of the load-bearing network of salt particles upon removal of the diluent phase.

The ability to obtain crack-free salt objects after the drying and sintering steps opens the way towards the manufacturing of complex-shaped structures for a variety of materials by simple infiltration and leaching of the salt template. To illustrate this process, we generated a salt object with a complex gyroid geometry and used it as a template to create polymer scaffolds with unique 3D architecture (**Figure 4**a). The fidelity of the manufacturing process is evaluated by performing microcomputed tomography (microCT) of the salt-based object after each of the printing, sintering, and infiltration steps.

Digitally visualized cross-sections obtained from the microCT of the object demonstrate that the manufacturing process preserves with high fidelity the morphology of the original digital design throughout each of the multiple steps. Importantly, the shrinkage of the object along the process needs to be considered in the original design to reach the desired final dimensions. Because of the layer-by-layer nature of the printing process, the object was found to shrink predominantly along the vertical (z) direction during the post-printing drying and sintering steps. This is well in-line with previous sintering studies of particle-based SLA printing.[41,42] Linear shrinkage in the z-direction reached 27.9% after complete heat treatment, as opposed to a value of 19.1% along the x- and y-directions (Figure 4a, bottom). The observed shrinkage can be beneficial for the fabrication of complex structures with dimensions below the resolution limit of the printer.

The open porosity of the chosen gyroid structure allows for facile infiltration of the sintered salt template by simple casting of a thermally curable resin or injection-molding of a molten polymer. We demonstrate the compatibility of our developed salt templates with these two infiltration approaches using commercially available biomedical silicone resin and thermoplastic polycaprolactone (PCL). MicroCT images of the resulting infiltrated and leached silicone scaffold indicate minimal shrinkage of the object and the formation of a pore-free polymer phase within the interstices of the leached salt structure. Upon leaching in water at room temperature, we obtained porous silicone and PCL scaffolds with exquisite and complex 3D architecture (bright-field image in Figure 4b).

Scaffolds with such digitally programmable pore size and morphology are highly desired for the ingrowth of cells and tissues in biomedical applications. Since the material of interest is directly infiltrated into the salt, it does not contain unreacted monomers or additional chemicals typically required for the light-based printing of polymers. This beneficial feature allows for the fabrication of complex-shaped biocompatible structures without toxic residues that could be harmful to living cells. While salt templating is often used to fabricate bio-scaffolds, the poor geometrical control over the pore structure of existing processes challenges the cell seeding efficiency and vascularization thereof.

To demonstrate the suitability of our process in fabricating scaffolds for biomedical applications, we measured the viability of pre-osteoblast cells on silicone and PCL scaffolds displaying a gyroid structure with distinct pore sizes in the range of 150–500 µm (Figure 4b). Before cell seeding, the scaffold surfaces were pretreated to promote cell adhesion with either fibronectin or sodium hydroxide for the silicone and PCL scaffolds, respectively. The results obtained after 2 days of culture show cell viability higher than 94% for all the scaffolds tested, confirming the cytocompatibility of the polymer structures and their suitability for in vitro cell culture. In light of the latter, preosteoblast cells were observed to spread homogeneously over the scaffold surface and to easily penetrate into the open porous architecture.

Beyond silicone and PCL, a broad range of materials can be shaped into complex architectures using the proposed manufacturing platform. We demonstrate this universal nature by creating intricate 3D structures from various materials as diverse as chocolate, aluminum, magnesium, carbon fiber composites, and degradable polymers (Figure 4c and Figure S7,

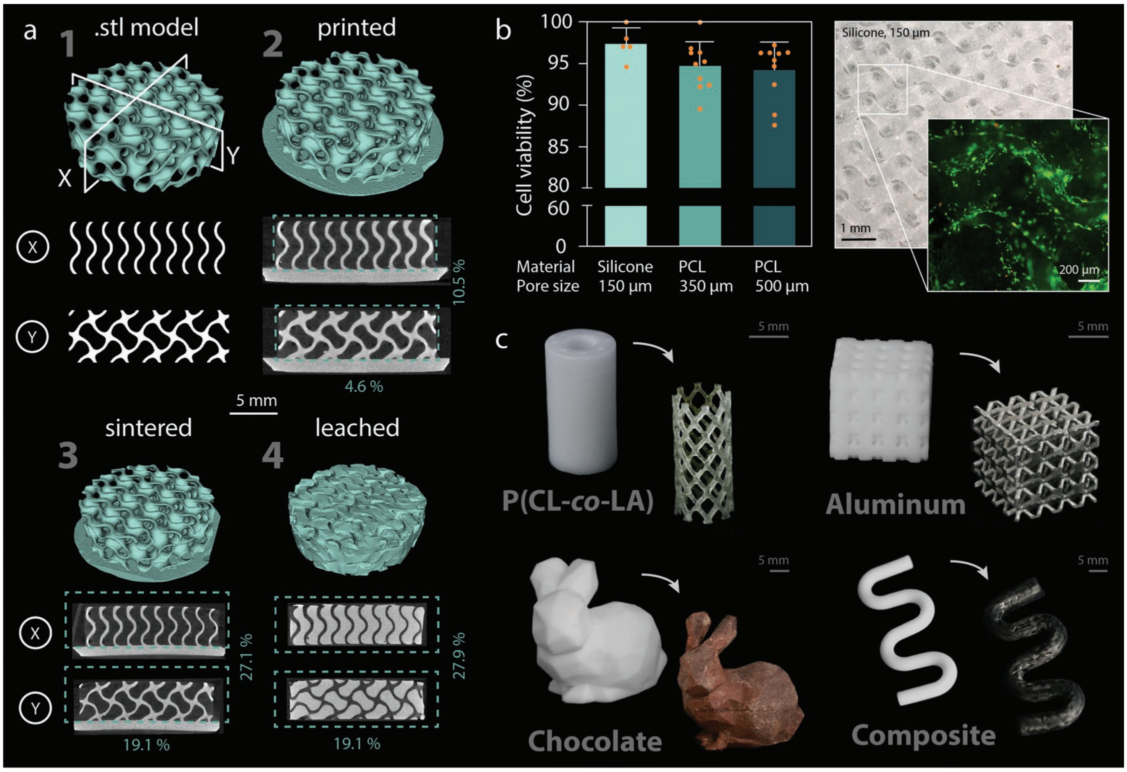

Figure 4. Complex-shaped structures made through infiltration and leaching of salt molds. a) Comparison of gyroid digital model (1) with microcomputed tomography (microCT) analysis of a printed (2), sintered salt template (3), and molded and leached silicone scaffold (4). X and Y denote specific cross-sections, as indicated in (1). The linear shrinkage along different directions is indicated (in blue) as a percentage of the initial digital model. The scale bar of 5 mm is valid for (1–4). b) Cell viability analysis of gyroid scaffolds prepared by leaching the 3D printed NaCl templates from infiltrated samples (either silicone or PCL). Left: Quantitative analysis of cell viability from live/dead assay on three different scaffold types made from silicone or PCL ($n = 5$–10). The cell viability is >94% 2 days after seeding for all three scaffolds. Right: Representative confocal laser scanning microscopy image showing live/dead assay results of MC3T3-E1 pre-osteoblasts that have been seeded on a fibronectin-coated silicone scaffold with a pore size of 150 µm (green: live, red: dead). c) Examples of sintered salt molds and the corresponding complex-shaped structures of a range of materials obtained after infiltration and leaching steps. Top left: tracheal stent made of bioresorbable poly(DLLA-*co*-CL) copolymer. Top right: ultralightweight octagon lattice made from an Al-Si 12.6% metallic alloy. Bottom left: edible bunny made from dark chocolate. Bottom right: hollow reinforced tube made by covering a salt core with a carbon fiber composite.

Supporting Information). We further demonstrate the process diversity by shaping these materials through infiltration into salt molds or intricate salt templates, or by warping salt cores. The complex mold geometries enabled by light-based printing allow shaping these materials into 3D structures that would be very challenging to achieve using conventional manufacturing technologies.

For example, biodegradable high molecular weight poly(D,L-lactide-*co*-ε-caprolactone) methacrylate (poly(DLLA-*co*-CL) MA) copolymers that are too viscous for light-based direct printing[5] were easily molded into stent-like geometries using printed salt templates (Figure 4c, top left). In another instance, lightweight aluminum lattices and bioresorbable magnesium with intricate porous architectures were manufactured by molten metal infiltration of salt templates at 710 and 700 °C, respectively. Even more elaborate hierarchical porous architectures can also be created by introducing salt particles within the material of interest before its infiltration step (Figure S7, Supporting Information). This plethora of examples demonstrate the potential of this light-based printing technology in leveraging salt templating for the shaping of so far inaccessible materials and geometries.

3. Conclusions

Here, we showed that using light-based printing of salt-laden resins, complex-shaped salt templates can be fabricated upon calcination and sintering. Such templates can be infiltrated and leached at room temperature in water to shape a broad range of materials with exquisite architectures. Careful design of the resin composition is crucial to enable printing of high-fidelity, crack-free templates. A salt particle concentration of 65 wt% was found to be optimal to minimize shrinkage of the template upon sintering while ensuring a sufficiently fluid ink during printing. In terms of shape fidelity, we observed that by tuning both photoinitiator and photo-absorber contents, salt objects with positive features down to 100 µm could be manufactured using light doses provided by a regular desktop stereolithographic printer. To generate defect-free objects, cracking of such objects during heat treatment should be avoided, imposing a common challenge in the field. Here, we demonstrated a strategy to reduce the internal stresses resulting from the differential shrinkage of the polymerized composites across the printed layer. In fact, we discovered that the addition of the non-reactive diluent camphor favors the formation of a load-bearing salt particle network within the ink upon its sublimation during drying that compensates for the differential shrinkage arising from polymerization gradients, and thus minimizes cracking of the printed object. Using this approach, crack-free salt templates can be successfully obtained and infiltrated with a broad range of materials by casting or injection molding. Since the salt phase is easily removed in water at room temperature, this manufacturing platform allows for the shaping of a wide variety of materials into unique complex geometries. In contrast to conventional injection molding and direct layer-by-layer printing, the use of printed salt molds in an indirect additive manufacturing workflow also enables cost-effective mass customization of complex-shaped objects without the defect-prone interfaces often created by additive manufacturing. These features open new opportunities for the design and fabrication of complex material architectures using a versatile, affordable, and sustainable manufacturing approach.

4. Experimental Section

Ink Preparation: Sodium chloride (NaCl), bis(2-ethylhexyl) sulfosuccinate sodium salt (AOT), and 2-propanol (99.8% purity) were all purchased from Sigma Aldrich. To decrease the size of the as-received particles to an average particle size below 2 μm, 50 g of NaCl and 0.875 g AOT (1.75 wt% with respect to NaCl, except noted otherwise) were dispersed in 100 mL of 2-propanol (99.8 %, Sigma-Aldrich). The dispersion was ball-milled in a planetary ball mill (PM100, Retsch GmbH) at 200 rpm for 2 h (including cooling breaks), at intervals of 5 min milling spaced by 5 min breaks. The milling was performed in a custom-made alumina jar using 575 g zirconia balls with diameters of 9.7, 7.6, 4.9, and 2.4 mm. The milled slurry was dried at 60 °C overnight. To form the photopolymerizable resin, the non-reactive diluent camphor ((1R)-(+), 98% Alfa Aesar), the photo-absorber Sudan I (Acros Organics), and the photoinitiator Omnirad 819 (iGM Resins) were fully dissolved in the monomers Isobornyl acrylate (IBOA, technical grade, Sigma Aldrich) and 1,1,1-trimethylolpropane triacrylate (TMPTA, technical grade, Sigma Aldrich). The monomers were used at an IBOA-to-TMPTA weight ratio of 85:15. The concentration of camphor is always indicated as weight percentage of the liquid phase. Photo-absorber and -initiator were added at 0.05 and 2 wt% with respect to monomer concentration, respectively (unless stated otherwise). To prepare the final ink, 65 wt% of milled NaCl particles were homogeneously dispersed in the photopolymerizable resin at 800 rpm for 10 min by using a planetary centrifugal mixer (Thinky Mixer ARE-250, Thinky Cooperation).

Rheological Characterization of NaCl Inks: The rheological properties of inks with varying salt, surfactant, and diluent concentrations were analyzed by viscosity measurements on a stress-controlled rheometer (Anton Paar MCR 302, Anton Paar GmbH). All measurements were performed at 25 °C with a parallel-plate setup using sand-blasted plates to minimize wall slip. The plates had a diameter of 25 mm and a gap size of 1 mm was employed. Steady-state measurements were performed by increasing the shear stress logarithmically from 0.01 to 200 Pa. The yield stress was defined as the point of sudden increase of shear stress in a double logarithmic shear strain versus shear stress representation of the data.

3D Printing of NaCl-Based Inks: Commercially available software and hardware were used for file generation and printing. Digital models were drawn using Fusion 360 (version 2.0.11894, Autodesk) or Rhino 7 (Rhinoceros) with the plugin Grasshopper. The objects were sliced with PrusaSlicer (version 2.3.3+x64, Prusa Research) and printed on an LED-LCD printer (SL1, Prusa Research). Aluminum foil (common household foil) was used to cover the printhead building area to facilitate part detachment after printing. The light intensity of the printer was pre-set to 0.1 mW cm^{-2}. To analyze the influence of photoinitiator and photo-absorber on the degree of polymerization, rectangular areas (9.7 mm × 8 mm) of the ink were freely illuminated without the constraint of the print head in z-direction for varying durations in multiples of 2 s (up to 32 times). After the removal of uncured resin with 2-propanol, the thickness of each square was determined with a micrometer screw gauge. A minimally required exposure time to reach 80 μm cure depth was calculated from the resulting light penetration depth (h_a) and critical energy dose (D_c) for each ink individually. In order to increase the adhesion at the printhead, the initial layers were exposed for 30–50 s with 10 fading layers to reach the desired illumination time. The layer thickness was fixed at 50 μm, unless stated otherwise. The print accuracy of negative and positive features was analyzed for various photo-absorber concentrations to investigate its role in the attainable resolution. All inks were printed under exposure conditions to reach a targeted cure depth of 80 μm. Negative holes of varying diameter were printed in a 2 mm solid bar, parallel to the build plate. Positive bars of varying width and 1 mm height were printed on a baseplate. The samples were visualized with a Keyence microscope and the resulting images analyzed with ImageJ (ImageJ2, version 2.3.0/1.53f). Three measurements were conducted for each data point. Digital designs were oversized by 15% in the x- and y-direction, and 25% in the z-direction to compensate for the shrinkage due to the heat treatment. After printing, the samples were cleaned with 99.8 % pure 2-propanol by 3 × 3 min sonication in an ultrasonic bath. The samples were further dried at ambient conditions before characterization.

Pyrolysis and Sintering of Printed Structures: Thermogravimetric analysis (TGA) and differential scanning calorimetry (DSC) analysis were performed to determine the appropriate pyrolysis and sintering profile (TGA/DSC 3+, Mettler Toledo). Printed samples were weighted in a lid-covered Al_2O_3 crucible (70 μL) while heated between 25 and 600 °C at a heating rate of 2 °C min^{-1} in air. Pyrolysis and sintering were further performed in a single temperature treatment in a Nabertherm LT furnace. In the first step, the samples were heated from room temperature to 200 °C at 0.67 °C min^{-1}. The temperature was then kept at 200 °C for 4 h to remove volatile organic residues such as the non-reacted monomer and the diluent. The temperature was afterwards further increased to 350 °C at 0.25 °C min^{-1} and held at 300 °C for 4 h. To complete the pyrolysis of the polymerized polymer matrix, the samples were further heated to 450 °C at 0.25 °C min^{-1} and kept constant thereafter for another 4 h. Finally, sintering was performed by increasing the temperature to 690 °C at 1 °C min^{-1}. Full densification was obtained by holding the sintering temperature for 4 h. The measurement was performed with an empty reference crucible, and calibrated with a blank curve measurement.

SEM Sample Preparation and Imaging: All samples for scanning electron microscopy (SEM) imaging were mounted on a carbon sticker. For improved electron conductivity, the samples were sputter-coated with 7–8 nm Pt (CCU-010, Safematic GmbH). The images were acquired on a Leo 1530 Gemini (Zeiss) SEM using an in-lens detector and an acceleration voltage of 5 kV.

Nitrogen Gas Sorption Analysis: Nanoporosity, pore-size distribution, and surface area were determined by nitrogen gas sorption at 77 K on a Quantachrome Autosorb iQ. The samples were outgassed for at least 24 h. The outgassing temperature was set to 30 °C for samples without any thermal treatment, or to 80 °C for previously heat-treated samples. Density functional theory (DFT) analysis was used to determine the pore size and volume. The calculations were performed using a non-local DFT (NLDFT) sorption model based on N_2 adsorption on cylindrical silica pores at 77 K. The surface area was determined by the Brunauer–Emmett–Teller (BET) method.

Evaluation of Crack Formation: Cubes of different side length (0.25–1 cm) were printed as described previously. All cubes were printed with a targeted cure depth of 80 μm and post-processed as described above. No cracks were observed for any of the cubes after printing and cleaning. For the first heating step, the cubes were heated to 200 °C at 0.67 °C min^{-1} in a Nabertherm LT furnace. The temperature was then held at 200 °C for 4 h, before cooling freely back down to room temperature (no active cooling or heating). For the second heating step, the samples were heated up to 200 °C at 3.3 °C min^{-1} to allow for the continuation of the thermal treatment as described above. After each heating step, the samples were imaged optically in transmission on an optical microscope (Keyence, VHX-5000, Keyence). The images were analyzed by determining the pixel ratio of crack area (white in transmission micrographs) to cube side area in ImageJ (ImageJ2, version 2.3.0/1.53f). Since the samples were intrinsically anisotropic due to the layered build-up approach of 3D printing, only the planes of the cubes parallel to the z-axis were considered. These 4 sides showed the largest cracking due to the reduced material strength at the layer interface. All measurements were performed in triplicates.

Warpage of Single Layers: The inks were individually exposed to light for 40 s in strips with a dimension of 20 mm × 5 mm. No printhead was used, allowing the light to freely propagate through the ink or resin. The printed layers were wiped with a damp tissue with 2-propanol to remove unreacted ink. The samples were dried overnight (dried) and finally placed into the oven for the heat treatment at 200 °C. The oven was heated from room temperature to 200 °C in 1 h, followed by an isothermal hold at 200 °C for another hour. Finally, the samples were left to cool back to room temperature.

Dynamic Mechanical Analysis (DMA): In order to perform dynamic mechanical analysis (DMA), rectangular samples with a length of 40–45 mm and a width and height of 25 mm were printed. The samples were printed on supports to eliminate any influence of increased light exposure of the first layers during printing. The measurements were conducted on a rotational rheometer (ARES-G2, TA Instruments) in nitrogen atmosphere by applying a constant torsional frequency of 3 Hz and an oscillation strain of 0.1%. The rheometer was equipped with an environmental test chamber and a torsion fixture for rectangular samples. In the first interval, the temperature was ramped at 2 °C min^{-1} from 30 to 230 °C. The temperature was further kept constant at 230 °C for 20 min in a second interval. Over the course of both intervals, the storage (G') and loss (G'') moduli were monitored.

Microcomputed Tomography (MicroCT): MicroCT was performed on one sample of a dried and sintered gyroid template, as well as on the corresponding cast and leached silicone scaffold, using a MicroCT100 instrument (Scano Medical AG). The scans were performed with an energy level of 55 kVp (peak kilovoltage), an intensity of 8 W, an exposure time of 139 ms, and a nominal resolution of 10 µm. The data was analyzed in 3D Slicer (version 4.11.20210226, http://www.slicer.org).

Cell Culture and Live & Dead Assay: Mouse pre-osteoblast cells (MC3T3-E1) were obtained from the University of Zurich, Zurich, Switzerland. The cells were used in passage number 31. First, 5×10^4 cells were seeded onto the scaffolds that were beforehand immersed in a fibronectin solution (Human Plasma Fibronectin Purified Protein, Sigma-Aldrich, FC010, 0.01 mg mL^{-1} in sterile phosphate buffered saline (PBS)) for 3 h. After allowing cells to attach for 2 h, growth medium composed of Minimum Essential Medium (MEM) α without ascorbic acid (Gibco, A1049001), 10% fetal bovine serum (Gibco, 26140079), and 1% antibiotic-antimycotic (Gibco, 15240062) was added to the cell culture. After 2 days of culture, the scaffolds were washed with PBS and the cells were stained for 10 min in 0.5 µL mL^{-1} calcein acetoxymethyl ester (calcein-AM) and 2 µL mL^{-1} ethidium homodimer-1 from the Live/Dead assay kit (Invitrogen, L3224). This was followed by cell fixation in 4% paraformaldehyde (Santa Cruz Biotech, 281692) for 15 min before washing again with PBS. Finally, confocal laser scanning microscopy (Zeiss, LSM 780 upright) was used to visualize the cells. Cell viability was calculated as the number of live cells divided by the total number of cells.

Preparation of Complex-Shaped Structures: All salt templates and cores were prepared as described above. Complex-shaped structures were generated by casting or infiltration of the salt templates following different procedures depending on the chemical and physical nature of the infiltrating material. Polymeric stent—The pre-polymers of randomly polymerized D,L-lactide (DLLA) and ε-caprolactone (CL) further functionalized by methacrylation were prepared as previously reported.[5] In short, a four-armed copolymer of 15 000 g mol^{-1} and a linear copolymer of 650 g mol^{-1} were synthesized using a monomer ratio CL/DLLA of 7/3 and 2/2, respectively. The obtained copolymers were mixed by combining 75 wt% four-armed and 25 wt% linear molecules. This pre-polymer mixture and 3 wt% of initiator (TPO-L, Speedcure) were heated to 60 °C to decrease the viscosity and facilitate homogenization. The resulting photosensitive resin was manually pressed into the sintered salt mold and cured by UV-light (Omnicure S1000, Lumen Dynamics) for 3 × 10 min. The mold was finally dissolved in water. Aluminum lattice—The salt templates were infiltrated as described previously.[43] A refractory crucible with the NaCl templates and a piece of AlSi 12.6 wt% aluminum alloy was heated to 710 °C under vacuum. After a holding time of 30 min, an Ar pressure of 1.5 MPa was applied to enable molten metal infiltration. Finally, the directionally cooled samples were cut to gain access to the NaCl templates, which were subsequently leached in water. Chocolate bunny—Swiss dark chocolate was molten, filled into the salt mold, and placed into the fridge for full solidification. The mold was dissolved in ice-water to prevent the chocolate from re-melting. Carbon fiber composite—The printed and heat-treated NaCl cores were wrapped with two layers of a braided carbon fiber sleeve (5 mm diameter, Suter Kunststoffe AG), infiltrated with a low viscosity epoxy resin (EPIKOTE Resin MGS, Suter Kunststoffe AG) and cured at room temperature with a shrink tape for compression (R&G Filament 160, Suter Kunststoffe AG) before final leaching in water.

Supporting Information

Supporting Information is available from the Wiley Online Library or from the author.

Acknowledgements

The authors thankfully acknowledge the financial support from the Swiss National Science Foundation (SNSF) through Sinergia (Project number CRSII5_177178). The authors further thank Prof. Christoph Brändli and Nicolai Jenal from the ZHAW School of Engineering for their kind support with the polymer injection molding and Robin Bergande, Muriel Haug, Lukas Hauser, and Dr. Murielle Schreck for their support in the laboratory. Furthermore, the authors wish to thank Dr. Elena Tervoort for her advice on the gas sorption experiments, and Dr. Kirill Feldman for conducting the dynamic mechanical analysis of the printed samples Finally, the authors thank Dr. Wilhelm Woigk for his support in the preparation of the composite demonstrator and Dr. Baris Kumru from TU Delft and Dr. Rafael Libanori for their kind inputs on the chemical reaction schemes.

Conflict of Interest

N.K., S.F., M.C., K.M., and A.R.S have filed a patent application related to this work.

Data Availability Statement

The data that support the findings of this study are available from the corresponding author upon reasonable request.

Keywords

additive manufacturing, sacrificial templating, salt printing, stereolithography

Received: April 29, 2022
Revised: June 9, 2022

[1] C. Minas, D. Carnelli, E. Tervoort, A. R. Studart, *Adv. Mater.* **2016**, *28*, 9993.
[2] E. Johansson, O. Lidstrom, J. Johansson, O. Lyckfeldt, E. Adolfsson, *Materials* **2017**, *10*, 138.
[3] E. A. Guzzi, G. Bovone, M. W. Tibbitt, *Small* **2019**, *15*, 1905421.
[4] J. Dong, Y. Li, P. Lin, M. A. Leeflang, S. van Asperen, K. Yu, N. Tumer, B. Norder, A. A. Zadpoor, J. Zhou, *Acta Biomater.* **2020**, *114*, 497.
[5] N. Paunovic, Y. Y. Bao, F. B. Coulter, K. Masania, A. K. Geks, K. Klein, A. Rafsanjani, J. Cadalbert, P. W. Kronen, N. Kleger, A. Karol, Z. Luo, F. Ruber, D. Brambilla, B. von Rechenberg, D. Franzen, A. R. Studart, J. C. Leroux, *Sci. Adv.* **2021**, *7*, eabe9499.
[6] D. W. McOwen, S. M. Xu, Y. H. Gong, Y. Wen, G. L. Godbey, J. E. Gritton, T. R. Hamann, J. Q. Dai, G. T. Hitz, L. B. Hu, E. D. Wachsman, *Adv. Mater.* **2018**, *30*, 1707132.
[7] A. Paolini, S. Kollmannsberger, E. Rank, *Addit. Manuf.* **2019**, *30*, 100894.
[8] Y. F. Zhang, C. J. X. Ng, Z. Chen, W. Zhang, S. Panjwani, K. Kowsari, H. Y. Yang, Q. Ge, *Adv. Mater. Technol.* **2019**, *4*, 1900427.
[9] Z. Q. Dong, H. J. Cui, H. D. Zhang, F. Wang, X. Zhan, F. Mayer, B. Nestler, M. Wegener, P. A. Levkin, *Nat. Commun.* **2021**, *12*, 247.
[10] N. Kleger, C. Minas, P. Bosshard, I. Mattich, K. Masania, A. R. Studart, *Sci. Rep.* **2021**, *11*, 22316.
[11] S. Gantenbein, K. Masania, W. Woigk, J. P. W. Sesseg, T. A. Tervoort, A. R. Studart, *Nature* **2018**, *561*, 226.
[12] D. G. Moore, L. Barbera, K. Masania, A. R. Studart, *Nat. Mater.* **2020**, *19*, 212.
[13] T. D. Ngo, A. Kashani, G. Imbalzano, K. T. Q. Nguyen, D. Hui, *Composites, Part B* **2018**, *143*, 172.
[14] E. Davoodi, H. Montazerian, A. Khademhosseini, E. Toyserkani, *Acta Biomater.* **2020**, *117*, 261.
[15] I. Capasso, B. Liguori, L. Verdolotti, D. Caputo, M. Lavorgna, E. Tervoort, *Sci. Rep.* **2020**, *10*, 612.
[16] J. H. Shin, J. H. Heo, S. Jeon, J. H. Park, S. Kim, H. W. Kang, *J. Hazard. Mater.* **2019**, *365*, 494.
[17] T. L. Nguyen, M. P. Staiger, G. J. Dias, T. B. F. Woodfield, *Adv. Eng. Mater.* **2011**, *13*, 872.
[18] S. Zekoll, C. Marriner-Edwards, A. K. O. Hekselman, J. Kasemchainan, C. Kuss, D. E. J. Armstrong, D. Y. Cai, R. J. Wallace, F. H. Richter, J. H. J. Thijssen, P. G. Bruce, *Energy Environ. Sci.* **2018**, *11*, 185.
[19] S. Mohanty, L. B. Larsen, J. Trifol, P. Szabo, H. V. R. Burri, C. Canali, M. Dufva, J. Emneus, A. Wolff, *Mater. Sci. Eng., C* **2015**, *55*, 569.
[20] Y. H. Jiang, Q. M. Wang, *Sci. Rep.* **2016**, *6*, 34147.
[21] F. Gallien, V. Gass, A. Mortensen, *Mater. Des.* **2022**, *215*, 110488.
[22] E. Sachs, M. Cima, P. Williams, D. Brancazio, J. Cornie, *J. Eng. Ind.* **1992**, *114*, 481.
[23] S. H. Deng, J. J. Wu, M. D. Dickey, Q. Zhao, T. Xie, *Adv. Mater.* **2019**, *31*, 1903970.
[24] J. J. Wu, J. Guo, C. H. Linghu, Y. H. Lu, J. Z. Song, T. Xie, Q. Zhao, *Nat. Commun.* **2021**, *12*, 6070.
[25] L. R. Meza, S. Das, J. R. Greer, *Science* **2014**, *345*, 1322.
[26] T. A. Schaedler, A. J. Jacobsen, A. Torrents, A. E. Sorensen, J. Lian, J. R. Greer, L. Valdevit, W. B. Carter, *Science* **2011**, *334*, 962.
[27] S. Mamatha, P. Biswas, D. Das, R. Johnson, *Ceram. Int.* **2019**, *45*, 19577.
[28] M. Dressler, S. Reinsch, R. Schadrack, S. Benemann, *J. Eur. Ceram. Soc.* **2009**, *29*, 3333.
[29] S. B. Lee, Y. H. Kim, M. S. Chong, S. H. Hong, Y. M. Lee, *Biomaterials* **2005**, *26*, 1961.
[30] Y. C. Chiu, J. C. Larson, A. IsomJr., E. M. Brey, *Tissue Eng., Part C* **2010**, *16*, 905.
[31] B. Nasri-Nasrabadi, M. Mehrasa, M. Rafienia, S. Bonakdar, T. Behzad, S. Gavanji, *Carbohydr. Polym.* **2014**, *108*, 232.
[32] T. G. Kim, H. J. Chung, T. G. Park, *Acta Biomater.* **2008**, *4*, 1611.
[33] K. Gorna, S. Gogolewski, *J. Biomed. Mater. Res., Part A* **2006**, *79a*, 128.
[34] Y. Conde, J. F. Despois, R. Goodall, A. Marmottant, L. Salvo, C. San Marchi, A. Mortensen, *Adv. Eng. Mater.* **2006**, *8*, 795.
[35] R. Goodall, A. Mortensen, *Adv. Eng. Mater.* **2007**, *9*, 951.
[36] N. Kleger, M. Cihova, K. Masania, A. R. Studart, J. F. Loffler, *Adv. Mater.* **2019**, *31*, 10.
[37] M. Schwentenwein, J. Homa, *Int. J. Appl. Ceram. Technol.* **2015**, *12*, 1.
[38] K. Y. Wang, W. Y. Pan, Z. Liu, T. J. Wallin, G. van Dover, S. Li, E. P. Giannelis, Y. Menguc, R. F. Shepherd, *Adv. Mater.* **2020**, *32*, 2001646.
[39] P. F. Jacobs, D. T. Reid, Computer, A. S. A. o. SME., *Rapid Prototyping & Manufacturing: Fundamentals of Stereolithography*, Society of Manufacturing Engineers, Southfield, MI **1992**.
[40] M. Hartmann, M. Pfaffinger, J. Stampfl, *Materials* **2021**, *14*, 1045.
[41] B. Coppola, J. Schmitt, T. Lacondemine, C. Tardivat, L. Montanaro, P. Palmero, *J. Eur. Ceram. Soc.* **2022**, *42*, 2974.
[42] F. Baino, G. Magnaterra, E. Fiume, A. Schiavi, L. P. Tofan, M. Schwentenwein, E. Verne, *J. Am. Ceram. Soc.* **2022**, *105*, 1648.
[43] H. P. Degischer, C. Körner, R. F. Singer, J. Banhart, F. Baumgärtner, G. Rausch, M. Arnold, M. Thies, C. San Marchi, A. Mortensen, O. Andersen, G. Stephani, in *Handbook of Cellular Metals*, Wiley, Hoboken, NJ **2002**, p. 5.